Research Square

Preprints are preliminary reports that have not undergone peer review.
They should not be considered conclusive, used to inform clinical practice,
or referenced by the media as validated information.

Ranking uncertainties in EGF near-fault strong motion predictions: Application to the Middle Durance Fault (France)

Elias El Haber

elias.el-haber@edf.fr

Electricité de France (EDF)-DT-TEGG

Mathieu Causse

Univ. Grenoble Alpes, Univ. Savoie Mont Blanc, CNRS, IRD, Univ. Gustave Eiffel

David Castro-Cruz

King Abdullah University of Science and Technology

Ludivine Saint-Mard

Electricité de France (EDF) - CIH

Fabrice Hollender

French Alternative Energies and Atomic Energy Commission (CEA), DES, CEA Cadarache

Research Article

Keywords:

Posted Date: September 1st, 2026

DOI: https://doi.org/10.21203/rs.3.rs-10700751/v1

License: This work is licensed under a Creative Commons Attribution 4.0 International License. Read Full License

Additional Declarations: No competing interests reported.

Abstract

This study addresses the need for reliable near-fault ground-motion predictions in low-to moderate seismicity regions, focusing on a Mw 6 scenario on the Middle Durance Fault. The objective is to identify and rank the main sources of uncertainty controlling amplitudes and durations in Empirical Green's Function (EGF) simulations. Ground motions are computed at two nearby stations—one located on rock and the other within a small sedimentary basin—using heterogeneous kinematic rupture models combined with a single EGF event. Results show that the overall variability of the simulated ground motions exceeds the typical total sigma reported by ergodic ground-motion prediction equations, highlighting significant epistemic uncertainties associated with EGF-based approaches. Using an ensemble machine-learning framework, we identify the EGF source parameters as the dominant contributors to variability. In particular, the EGF seismic moment and stress drop primarily control the ground motion motions, while the nucleation position of the main event has a secondary influence. Additional analyses combining three-dimensional numerical simulations of the main rupture with point-source simulations mimicking EGFs indicate that the impact of the configuration of the EGF dataset has a relatively small impact, mainly at frequencies below ~ 1 Hz. In this case, the spatial distribution of EGFs across the rupture area proves more important than their number. Notably, a single EGF located as close as possible to the station can already provide reliable predictions. Finally, comparison with the widely used Irikura-recipe EGF approach shows that methodological differences are small compared with the variability induced by uncertainties in the input parameters.

1. Introduction

Small earthquake recordings have been extendedly used to approximate the impulse response of the medium (or Green's function) for representing wave propagation in source and strong motion studies (e.g. review paper by Hutchings and Viegas, 2012). In such applications, small earthquake recordings are commonly referred to as Empirical Green's Functions (EGFs). In source studies, the analyzed earthquake recordings are generally deconvolved from the EGFs to extract some large scale properties of the source like stress drop, rupture velocity and/or rupture directivity (e.g. Mueller, 1985; Courboulex et al., 2013; Abercrombie et al., 2017; Chounet et al., 2018) or used to image the rupture propagation from finite-source inversion (e.g. Ross et al., 2017; Causse et al., 2017; Convertito et al., 2021; Zilic et al. 2025). In strong motion studies, the rupture is modeled and next combined with EGFs to synthetize surface ground motion for a large earthquake (e.g. Hartzell, 1978; Irikura and Kamae, 1994; Miyake et al., 2003; Kohrs-Sansorny et al., 2005; Fernández et al., 2021; Causse et al., 2023). Using EGFs is very attractive because the impulse response of the medium does not need to be numerically computed as EGFs naturally account for complex 3D wave propagation or site effects, under the assumption that the medium behaves linearly. Thus, ground motion observations can in principle be fairly well reproduced, even in complex geological structures like large 3D sedimentary basins where numerical simulations may fail predicting ground motion in a relevant frequency range for earthquake engineering applications (0.1–20 Hz) (e.g. Dujardin et al., 2016; Causse et al., 2017). The EGF technique has then been commonly used to simulate broadband ground motion for potential large earthquake scenarios (e.g. Causse et al., 2009; Honoré et al., 2011; Irikura and Miyake, 2011; Oral and Satriano, 2021).

For a small earthquake recording to be used as EGF, it must satisfy some basic requirements, namely: (1) share the focal mechanism of the target event; (2) be located on the rupture area of the target event; (3) have a flat source spectrum up to the maximum analyzed frequency f_{max}, so that the source-time function can be

considered as impulsive (i.e. delta-like) up to f_{max}. Such conditions are rarely satisfied and some correction procedures are generally necessary (stress drop, anelastic and geometric attenuation, radiation pattern). Regardless of the application, EGF-modeled ground motion depends on the choice of the EGFs set to some extent and the stability of the results needs to be tested considering various EGFs. For instance, the uncertainty in stress drop estimates of small earthquakes using EGF modeling of spectral ratios significantly decreases as more EGFs are available and if the EGFs are well correlated with the waveforms of the analyzed earthquake (e.g. Kane et al., 2011; Abercrombie, 2015). Regarding the prediction of strong ground motion, a sufficient number of EGFs is required to properly sample the rupture area of the simulated earthquake and represent the wave propagation between all the fault elements and the target station, especially in the near-fault region (i.e. at distances smaller than the rupture length). The EGFs must then be interpolated (corrected) to account for variations of distance between fault-elements and station, fault mechanism and EGF source parameters (e.g. Hutchings and Wu, 1990). The use of different EGFs sets can result in variable amplitude of predicted ground motion (e.g. Wossner et al., 2002; Del Gaudio et al., 2015; Courboulex et al., 2010). Besides, the EGF source parameters (seismic moment, stress drop) are generally associated with large uncertainties (e.g. Shearer et al., 2019), which propagate into the simulated ground motion (e.g. Pavic et al. 2000). This is even truer in low-to-moderate seismic areas, where EGF's are generally small events (typically M_w<3) and thus, robust estimates of moment magnitude and stress drop are difficult to obtain.

In addition to the uncertainty associated to the selection and processing of EGF, strong ground motion predictions for potential large events strongly depend on the choice of finite-fault source parameters, which are *a priori* unknown (Pavic et al., 2000; Liang and Hao, 2009). The variability due to the randomness of the rupture process (*i.e.* the variability among repeating earthquake ruptures for fixed magnitude and fault) is generally referred to as 'random variability' (*e.g.* Anderson and Brune, 1999) and is of the order of 0.2–0.5 (considering Peak Ground Acceleration - PGA), as reported by between-event variability analyses in Ground Motion Models (Cotton et al., 2013, where the variability is expressed as σ_{ln}(PGA)). This issue goes beyond the scope of EGF predictions and pertains to all simulation techniques of large event ground motions. Several studies analyzed the impact of different rupture scenarios on the resulting ground motion, including physically realistic values of the position of the rupture initiation, average rupture velocity, slip distribution on the fault and slip rate function using kinematic or dynamic rupture modeling (*e.g.* Causse et al., 2008; Ripperger et al., 2008; Ameri et al., 2009; Cultrera et al., 2010; Imtiaz et al., 2015; Parker et al. 2023; Čejka et al; 2024). The ground motion variability over various rupture scenarios is generally found to be the largest in the near-source region (*e.g.* Valentová et al., 2021), where strong ground motion depends on random local processes, including local stress drop, spatial variations of rupture velocity and local slip velocity (e.g. Spudich and Frazer, 1984; Schmedes and Archuleta, 2008; Fayjaloun et al., 2020). Finally, the choice of the method used to simulate the fault rupture process introduces an additional component to the global ground motion prediction uncertainty, referred to as 'model uncertainty' (*e.g.* Hartzell et al., 2011).

In low-to-moderate seismicity areas, the absence of strong motion recordings of significant earthquake makes it generally difficult to anticipate the effects of potentially damaging events. Although EGF-based simulations have been used for near-fault ground motion prediction as an alternative to Ground Motion Models, they generally rely on a very small number of EGFs, sometime a single one (*e.g.* Causse et al., 2009; Del Gaudio et al., 2018; Dujardin et al., 2020). There is thus a need to better quantify and hierarchy the various sources of uncertainties in such a context. In this paper, we use the Cadarache area (Southeast of France) as a case study for

investigating uncertainties in EGF-based near-fault ground-motion simulations considering a potential Mw 6 event on the Middle-Durance fault system (Fig. 1).

The Cadarache area was selected as a case study because it benefits from an unusually comprehensive dataset accumulated over the last two decades. These studies have led to the development of detailed three-dimensional geological and geophysical models of both the Middle Durance Fault system and the local subsurface structure (Guyonnet Benaize…). In addition, the area is instrumented by a seismological stations that has recorded numerous earthquakes in the vicinity of the fault since the early 2000s. This region is of particular interest for seismic hazard studies because it hosts several critical infrastructures, including nuclear research installations subject to dedicated seismic safety assessments. It experienced the 1909 Lambesc earthquake, with a M_w magnitude of 6.0 as reported by Baroux et al. (2003) and 5.7 according to the FCAT17 French seismic catalog by Manchuel et al. (2018). This event, that is not associated to the Middle Durance Fault, is one of the strongest earthquakes documented in mainland France during the historical period. In addition, the 4.7 magnitude earthquake that occurred in Manosque in 1708 (Manchuel et al., 2018), is considered as the strongest event associated to the Middle Durance Fault, aim of our study. Previous research proposed potential M_w 6.0 rupture scenarios on this fault system using kinematic fault modeling and empirical Green's functions (EGFs) (Dujardin et al. 2018, 2020) and blind 3D broad-band (0–10 Hz) numerical simulations (Castro-Cruz et al. 2021, 2023). The predicted ground motions of these empirical and numerical studies were found to be compatible with several ground motion prediction equations (GMPEs). In this study, we assume that the rupture area is fixed and predict ground motion at 2 nearby sites about 7 km from the fault within the Cadarache site, one at a rock site (CA02 station) and the other one being located within the small Cadarache 3D sedimentary basin (CA04 station) (Fig. 1). Using a single M_w 2.8 event as EGF, which occurred in 2010, the EGF-based method mainly used in this study, is based on a complex description of the rupture kinematics (Dujardin et al., 2020; Causse et al., 2021), and is referred to as 'KIN'. First, we use the 'KIN' method to analyze the influence of rupture parameters (random variability) and EGF parameters (epistemic uncertainty) on ground motion. We deploy an ensemble machine learning algorithm (bootstrap aggregation of regression trees) to estimate the importance of each parameter, providing a ranking of the model parameter influence. Next, we conduct 3D numerical simulations for a fixed rupture model (generated with the 'KIN' method) at the 2 sites, considered as reference solution. In addition, we simulate the medium impulse response for a set of 12 point-sources distributed over the fault plane, to obtain a set of synthetic Green's functions (SGFs). We then compute ground motion using the same rupture model and SGF summation, as would be done in a real-case scenario using recorded EGFs. Considering different sets of SGFs—ranging from the full set of 12 SGFs to a reduced subset or even a single SGF to mimic conditions in a low-seismicity area—we quantify the uncertainty in the predicted ground motion arising from the limited number of available EGFs. Finally, we compare ground predictions performed using 'KIN' method to ground motion predictions obtained from a more traditional method. This second method is known as the 'Irikura recipe' (Irikura and Miyake, 2011), referred to as 'IR' in the following. It has been excessively used for large fault ground motion prediction or recorded earthquake source parameter determination in Japan and considers the rupture process as a sum of a few slip asperities. This comparison allows us to better understand uncertainties related to the choice and the use of the EGF-based techniques.

Figure 1

Map of the Cadarache area (Southeast of France) showing an example of rupture scenario for a M_w6 event. The blue dots correspond to the 2010 and 2018 small earthquakes that occurred on the Middle Durance Fault system. Only the 2010 event, located within the assumed rupture area, is used as EGF. The numbered white dots correspond to the synthetic events (point source) generated using SEM3D, see section 6 for details. The white star and isolines correspond, respectively, to the epicenter and the rupture time of this scenario. Simulations are performed at stations CA02 (located at rock) and CA04 (located within the small sedimentary basin, represented in brown). The black dashed line represents the trace of the MDF (Guyonnet-Benaize et al. 2015).

2. EGF-based ground motion simulation using the KIN method

2.1 Brief overview of the 'KIN' method

In this study, an EGF simulation technique is used to predict ground motion at two stations: CA02 (rock site) and CA04 (soft site). It's the 'KIN' method developed and applied to the Middle Durance Fault by Dujardin et al. (2020). As with all the EGF-based techniques, this technique is based on a kinematic description of the fault as first described by Haskell (1964) and uses the small events recordings to predict large earthquakes ground motions.

The 'KIN' method combines the generation of heterogeneous distributions of kinematic rupture parameters with the use of EGFs to predict time series. The slip distribution is self-similar and is characterized by a k^{-2} decay for high wavenumbers, as commonly assumed (e.g. Andrews 1980; Herrero and Bernard 1994; Causse et al. 2009; Stone et al. 2025). The rupture time is also assumed to follow a k^{-2} distribution, while the rise time is constant over the fault plane. These choices ensure that the source spectrum is consistent with a ω^{-2} source model (Brune 1970). The EGFs are deconvolved from a Brune (1970) source model so that they can be treated as "true" Green's functions. The fault discretization is then set to ensure numerical stability in the summation process. For more details about this method, please refer to Dujardin et al. (2020).

Figure 1 shows the slip distribution of one scenario, generated using the KIN method (Dujardin et al., 2020), as well as the locations of stations CA02 and CA04, at hypocentral distances (R_{hyp}) of 17.8 and 16.7 Km, respectively. These stations are the only ones in the Cadarache basin (our case study) that recorded the 2010 small event used as EGF for our simulations in this study. They also recorded the 2018 small earthquake, but this event is far away from the simulated rupture (see Fig. 1) and hence will not be used as EGF in our calculations. Table 1 summarizes the main characteristics of the 2010 scenario.

2.2 EGF correction

In addition to the classical travel-time and geometrical spreading corrections (e.g., Irikura, 1986; Hutchings, 1994), a cutoff frequency (f_{max}) correction —originally applied in the IR method following the Irikura recipe— is also implemented in the KIN method, as explained below. Hanks (1982), based on observational data, identified a decay in the Fourier acceleration spectrum above a certain cutoff frequency, f_{max}, and proposed that this parameter reflects path or site effects. A similar interpretation was later supported by Anderson and Hough (1984). In contrast, several Japanese studies (e.g., Umeda et al., 1984; Faccioli, 1986; Aki et al., 1988; Fujiwara et al., 1989, 1991) suggested instead that f_{max} is primarily controlled by source properties. If f_{max} is indeed a source-controlled parameter, correction for f_{max} should be applied when scaling ground motions from a small

event to a target event. In this framework, the high-frequency decay, $HDF(f)$, is introduced to model the spectral attenuation beyond f_{max}. In the present study, $HDF(f)$ is represented using a Butterworth-type high-cut filter, following Boore (1983), expressed as:

$$HDF(f) = \frac{1}{\sqrt{1+\left(\frac{f}{f_{max}}\right)^{s}}} \quad \text{Eq. 1}$$

where f_{max} is the cut-off frequency and s is a power coefficient.

Then, EGFs are multiplied in the frequency domain, by $HDF_{target}(f)/HDF_{EGF}(f)$. Because the physical origin of the high-frequency decay remains debated, both configurations - with and without correction - are considered when using the 'KIN' method. For the 2010 event, f_{max} and s are estimated based on the recorded data, and are respectively equal to 22 Hz and 4 Hz. However, for the Mw6 target event, f_{max} is fixed to 6Hz and s to 2 (Tsururu et al., 1997).

Furthermore, following Pitarka et al. (2000), a frequency-dependent radiation pattern correction is incorporated into the KIN approach (Dujardin et al., 2020), whereas it is not included in the traditional Irikura recipe. To enable a direct comparison, the KIN simulations are conducted with and without this correction.

Table 1
2010 EGF metadata used in this paper

Event	Latitude (°N)	Longitude (°E)	Depth (km)	Strike (°)	Dip (°)	Rake (°)	ML/Mw	Mo (Nm)	Fc (Hz)	Fmax (Hz)
08/07/2010	43.84	5.781	3.49	186	19	-90	2.9/2.8	1.80E + 13	6.3	22

3. Ranking influence of input parameters in EGF ground motion predictions

Here we perform a suite of 5000 ground motion simulations for a Mw6 event using the 'KIN' model at the rock site CA02, considering variability in both the rupture scenarios and the EGF parameters. The fault plane is discretized to reach a maximum frequency of 10 Hz. The simulated ground motion time series are lowpassed filtered in the frequency range 1–10 Hz to ensure a signal-to-noise ratio of the EGF recordings larger than 3 (Dujardin et al. 2020). For each simulation, we compute the following ground motion indicators: PGA, SA(1Hz) and SA(3Hz). While the position of the rupture area is fixed as shown in Fig. 1, 5000 rupture scenarios are generated by considering variability in the average rupture velocity (V_R), the average stress drop ($\Delta\Sigma$) and the hypocenter position (defined by its along-strike and along-dip positions, X_{nuc} and Y_{nuc}, respectively). The probability distributions of V_R, X_{nuc} and Y_{nuc} are defined based on statistical analyses of databases of finite-source rupture models (Somerville et al. 1999, Mai et al. 2005), while the distribution of $\Delta\Sigma$ is inferred from observations of between-event variability of PGA coupled with simple relationship between $\Delta\Sigma$ and PGA (Cotton et al. 2013) (Table 2). Note that the spatial distributions of slip and rupture time are also variable since we consider random phases of their Fourier spectra (see section 2). In addition, in order to account for uncertainties in the EGF source parameters, the seismic moment (m_0) and EGF stress drop ($\Delta\sigma$) are also

assigned probability distributions, based on expert judgment (Pavic et al. 2000) (Table 2). The simulated ground motion indicators are all approximately log-normally distributed with a standard deviation $\sigma_{ln} \approx 1.0$, which corresponds to a factor of ~ 2.7. This is significantly larger than the between-event variability values commonly reported in Ground Motion Models, which are rather in the range 0.2–0.5 in log10 scale (*e.g.* Cotton et al., 2013).

Table 2
probability distributions used for assessing the impact of the input parameters on the ground motion

Input parameter	Type of distribution	Median value	Standard deviation	Reference
Rupture velocity (V_R)	Uniform between 2500 and 3000 m/s[!]	2750 m/s	0.05[▯]	Heaton 1990, Somerville et al. 1999
Stress drop ($\Delta\Sigma$)	Log-normal	3 MPa	0.4[▯]	Cotton et al. 2013
Along-strike hypocenter position (X_{nuc})*	Normal	0.5	0.23	Mai et al. 2005
Along-dip hypocenter position (Y_{nuc})*	Uniform between 0.5 and 1	0.75	0.2[▯]	Mai et al. 2005[+]
EGF seismic moment (m_0)	Log-normal	1.8e13 N.m	1.0[▯]	Pavic et al. 2000
EGF stress drop ($\Delta\sigma$)	Log-normal	1 MPa	1.9[▯]	Pavic et al. 2000

[!] This corresponds to values between about 70% and 90% of the shear wave velocity, consistent with the mentioned publications

* The along-dip and along-strike hypocenter positions have values between 0 and 1. Ynuc = 1 corresponds to a nucleation in the deepest part of the rupture

[+] We use a simplified distribution accounting for the fact that most of the ruptures nucleate at depth

[▯] For lognormal distributions, the standard deviations is computed on the natural logarithm values

In order to understand the origin of the uncertainty in the ground motion predictions, the influence of each parameter (including both the Mw6 rupture parameters and the EGF parameters) on the ground motion is then quantified via an ensemble machine learning algorithm. First we use the *fitresemble* function of the Matlab's Statistics and Machine Learning Toolbox™ to obtain a bootstrap aggregation (bagging) of regression trees (Breiman, 1996), which can be employed to perform predictions of the output variables (*PGA, SA(1Hz), SA(3Hz)*)) from the predictors *(V_R, $\Delta\Sigma$, X_{nuc}, Y_{nuc}, m_0, $\Delta\sigma$)*. The hyperparameters (number of trees, maximum number of branch nodes, minimum number of leaf node observation) are optimized using Bayesian optimization. The prediction performance is characterized using the out-of-bagg prediction (that is the average over predictions from individual trees, in which each tree is trained from a random subset containing on average 63% of the complete dataset, the remaining out-of-bagg dataset being used to assess the prediction performance). The performance is expressed as the coefficient of determination between the out-of-bagg predictions and the out-of-bag observations. Finally, we compute the out-of-bag importance of the predictors (using the *ooobPermutePredictorImportance* Matlab function), which measures how influential the predictors are at predicting the response. The influence of a predictor increases with this measure. The general idea is to

compare the out-of-bag predictions with predictions obtained by randomly permuting the values of the predictors. If a predictor is not influential, then permuting its values should have no effect on the model error and its importance equals 0. Note that the importance of any predictor depends on its uncertainty level and on the sensitivity of the output to the predictor. Thus, the importance provides a way to quantify and hierarchy the influence of the rupture and EGF parameters on the simulated ground motion.

The obtained importance values are shown on Fig. 2. First the values of the coefficient of determination R^2 range from about 0.7 to 0.9, indicating that the ensemble of regression trees performs robust predictions of the ground motion indicators. The R^2 value is the smallest for PGA because it is more sensitive to small-scale variations of the distributions of slip and rupture times - which are not included in the predictors - than the other ground motion indicators. While the PGA is dominated by high frequencies (up to 10 Hz), the values of SA(1Hz) remain primarily controlled by frequencies around 1Hz. Besides the results indicate that the most influential predictor is m_0 for all the ground motion indicators (Fig. 2a), which corroborates the sensitivity study by Pavic et al., 2000. In the EGF source deconvolution process, the EGF spectrum is normalized by m_0. Thus, a perturbation by a factor α of m_0 results in a perturbation by a factor α of any ground motion indicator characterizing the ground motion amplitude. The influence of the other predictors strongly depends on the frequency range of the ground motion indicator. Although Δσ also has a strong influence on PGA, it is very little influential on SA(1Hz). This is because the Δσ values are used in the EGF source deconvolution process and pertains only frequencies larger than the average EGF corner frequency, which equals 6.3 Hz. Finally, the M_w6 rupture parameters have approximately similar importance. Nevertheless, it is noticeable that the influence of X_{nuc} (and hence rupture directivity) increases as the frequency range of the ground motion indicator decreases (that is for PGV and SA(1Hz)).

In the aforementioned test, the influence of any input parameters on the ground motion depends on its uncertainty level and on the ground motion sensitivity to the parameters. As such, the test does not provide the origin of the importance value. For instance, the large importance obtained for the EGF seismic moment may arise because it is affected by particularly large uncertainty or because small perturbations of its value significantly change the ground motion, relatively to the other parameters. We then conduct a second set, in which all the predictors are assigned a uniform distribution with a coefficient of variation set to 0.18, while keeping the same median values (note that for a uniform distribution, the coefficient of variation is approximately equal to the standard deviation on the natural logarithm values). Since the uncertainty level is the same for each parameter, the importance value then reflects the sensitivity of the ground motion to the considered parameter (Fig. 2a). The results are shown on Fig. 2b. The values of R^2 are smaller than in the previous test (Fig. 2). This is because the chosen variability of the predictors is generally smaller and their contributions to the overall ground motion variability are then weaker. Figure 2b reveals that V_R has the highest importance - especially for PGA and SA(3Hz), which indicates that the ground motion indicators are mostly sensitive to the rupture velocity. The PGA is particularly sensitive to V_R in near-fault strong motion simulations - especially in case of forward directivity effects, in which PGA is often generated by abrupt variations of V_R at the rupture edges (e.g. Fayjaloun et al., 2020). Furthermore, the EGF seismic moment still has strong values of importance, while the remaining predictors have second order effects. Noticeably, ground motion is more sensitive to Y_{nuc} than X_{nuc} in the considered source-station configuration. This may be due to the low fault-dip angle, which tends to generate mainly up-dip rupture directivity.

4. Impact of the EGFs number on predicted ground motion

Next, we conduct 3D numerical simulations for a fixed rupture model at the 2 sites, considered as reference solution. The rupture model is generated with the 'KIN' method and is shown on Fig. 1. We consider both strike-slip and normal fault mechanisms (rake angle values of 0° and − 90°, respectively). The numerical model uses Spectral Element Method (Faccioli et al 1997, Komatitsch and Vilotte 1998) implemented in a High-Performance numerical code called SEM3D (CEA, CentraleSupélec, IPGP and CNRS 2017). The method is detailed in Castro-Cruz et al. (2021), who used the same code, combined with EGFs hybrid to develop hybrid ground motion prediction for the Cadarach site. Our numerical model uses the same geological and source information. This model meshes the region of Cadarache with ~ 5.9 million linear hexahedra elements for a total of 5.9x109 Degrees of Freedom (DOFs). At the boundaries of the models, a Perfectly Matched Layers (PML) absorbing boundary conditions were applied (Festa G, Vilotte JP, 2005). The mesh solves with high accuracy the wave-propagation problem up to a frequency of 8 Hz. The elements have a minimal length of 105.8 m outside the basin zone, and 45.7 m inside.

Furthermore, we simulate the medium impulse response for a set of 12 point-sources distributed over the fault plane and considered as synthetic EGFs, as indicated on Fig. 1. We next compute ground motion from the reference rupture model of Fig. 1 but using EGF summation with various sets of synthetic EGFs, so as to quantify the uncertainty due to a limited number of EGFs on the predicted ground motion. We synthetize ground acceleration considering the 12 synthetic EGFs, a set of 4 EGFs distributed over the whole fault plane, or single EGF. The comparison between the reference ground accelerations and predictions based on the set of 13 synthetic Green's functions, represented as time histories and response spectra, indicate on overall good level of fit (Fig. 3). To evaluate the extent of similarity between the reference and EGF synthetics, we use the criterion proposed by Maufroy et al. (2015) in the framework of a verification and validation project of 3D numerical simulations (Fig. 4). This criterion relies on an ensemble of ground motion parameters sensitive to various characteristics of the waveform: (1) Peak Ground Acceleration (PGA); (2) elastic response spectrum (SA) averaged over 1-2.5 Hz; (3) elastic response spectrum averaged over 0.3-1 Hz; (4) cumulative absolute velocity (CAV); (5) significant duration (RSD). Note that the first 3 criteria are computed considering the horizontal direction that maximizes ground acceleration. For each criterion, the misfit δ_P is expressed as:

$$\delta_P = \left(\frac{\log(P_{pred.}/P_{target})}{\log(2)} \right) \times 100. \quad \text{Eq. 2}$$

As such, negative values of δ_P indicate an underestimation of the reference, while positive values indicate an overestimation. As an example, δ_P=-50%, δ_P=-100% and δ_P=-200% indicate underestimation of 40%, 100% and 400%, respectively. The results indicate a fairly good level of similarity ($|\delta_P|$ of 50–100% for the 5 criteria) for both stations CA02 and CA04 and both fault mechanisms as the whole set of 12 synthetic EGF or 4 EGF (labels 6,7,9 and 11) are used. The level of similarity is also good when the closet EGF to the stations (labeled 11) is used as the sole synthetic EGF. In addition, Fig. 5 shows the comparison between the time histories and the response spectra when EGF 11 is used. On the other hand, the similarity is generally worse when other EGFs are used alone, especially if they are located at depth and far away from the stations.

5. Impact of the EGF methods: comparison between KIN and IR approaches

In this section, we compare the ground motions generated by the two different EGF-based methods to assess the impact of the methodological choices on the results. The first one is the ‘KIN’ method used so far in this study (see section 2) and the second one is Irikura recipe widely used in the literature.

5.1 Brief overview of the 'IR' method

The ‘IR’ method mainly developed by Irikura and Miyake (2011), largely used in Japan for seismic safety assessment (HERP 2017) and validated for large earthquakes (e.g. Irikura et al. 2004 for the 1995 Kobe and 2003 Tokachi-oki events).

The ‘IR’ method is based on the summation of EGFs within a kinematic source model, as proposed by Hartzell (1978). On the contrary to the 'KIN' method, the similarity’s relations between small and large earthquakes proposed by Kanamori and Anderson (1975) are then used to constrain the EGF summation process, which has been improved over the years (Irikura 1983, 1986; Irikura and Kamae 1994). Irikura and Miyake (2010) further enhanced the simulation method by introducing a "recipe" for determining source model parameters for broadband ground-motion simulations. This characterized source model includes strong motion generation areas, or asperities, with high stress drop and slip, and background slip areas with lower stress drop and slip. The source model is fully characterized using theoretical and empirical relations based on the fault length or moment magnitude. The specificity of this method compared to other kinematic simulations remains in the way to (1) sum up small events in order to obtain a larger event (2) characterize the source using asperities to represent heterogeneity in slip distribution.

5.2 Comparison between the ‘IR’ and ‘KIN’ methods

To focus only on the methodological choices, a single rupture scenario is used to simulate a Mw6 event on the Middle Durance Fault and compare the ‘IR’ and ‘KIN’ methods. Table 3 summarizes the main characteristics of this rupture scenario. As shown in Fig. 1, this rupture is located within the northwest dipping segment of the active fault zone documented by Guyonnet-Benaize et al. (2015). It corresponds to one of the four slip model proposed by Castro-Cruz et al. (2023), selected based on its proximity to both the 2010 EGF event and the CA02 and CA04 sites. Finally, to ensure a signal-ratio above 3, the simulations are performed in the frequency-band [1–35 Hz] (Dujardin et al., 2020).

Table 3
main rupture characteristics of the rupture scenario used for the two simulation techniques.

Rupture Parameters	**Values**
Moment magnitude	6 (Mw)
Epicenter location	5.6964°, 43.8229°
Hypocenter depth	4.42 km
Rupture dimensions (KIN method)	135 km^2
Rupture dimensions (IR method)	229 km^2
Strike	37°
Dip	23°
Rake	-90°
Stress drop	0.79 MPa
Rupture velocity (Vr)	2730 m/s
Rise time (KIN method: Somerville et al. 1999)	0.45 s
Rise time (IR method: HERP 2017)	0.78 s
Geometric spreading parameter (β)	1.06 (Dujardin et al. 2020)

In this study, the two EGF-based simulation approaches are implemented, each offering a range of user-selectable input parameters and correction options. For example, in both methods the rise time is assumed to be spatially uniform over the rupture area; however, it is defined differently in each approach. In the KIN method, the rise time follows the scaling relationship proposed by Somerville et al. (1999), yielding Trise = 0.45 s for a Mw6.0 event. In contrast, in the IR method it is defined according to the recipe of the Headquarters for Earthquake Research Promotion (HERP, 2017), resulting in Trise = 0.78 s. In addition, the rupture area is derived from the seismic moment, and the stress-drop but differs between the two methodologies. The ‘IR’ method uses the relationships by Kanamori and Anderson (1975) and Eshelby (1957), resulting in a rupture area of about 229 km². In contrast, the ‘KIN’ model uses the source model by Brune (1970) to obtain the corner frequency and the rupture duration and then infers the rupture dimension given the rupture speed (Dujardin et al. (2020), resulting in a shorter rupture area of about 135 km². Regarding the slip distribution, the IR method allows the generation of asperities and background slip parameters following the Irikura recipe (i.e., prescribed average slip and stress drop), whereas in the KIN approach the spatial distribution of the main slip patches is controlled by random phase realizations.

To better understand the origin of the differences in the simulated ground motions, four configurations are considered for each method. These configurations follow either the Irikura recipe recommendations, or the parameter choices described by Dujardin et al. (2020), and consider various EGF correction options, as summarized in Table 4. Notably, Fig. 6b presents the slip distribution adopted for the IR method, composed of

two rectangular asperities constructed to best approximate the KIN slip distribution shown in Fig. 6a. Note also that simulations 'KIN03' and 'IR04' in Table 4 have the same EGFs corrections.

Figure 6c and Fig. 6d present the moment-rate functions in the time and frequency domains, respectively, for the two methodologies considering rupture area and rise time consistent with the KIN parameterization (model KIN01 in Table 4). The moment-rate functions obtained using the IR method exhibit slight differences between stations CA02 and CA04 due to the introduction of random fluctuations in rupture time from one simulation to another. Nevertheless, they remain very similar to the moment-rate function generated by the KIN method. Moreover, the resulting spectra closely follows the classical ω^{-2} source model proposed by Brune (1970), as illustrated in Fig. 6d.

Table 4
user-selectable inputs and correction options considered for the calculations using the 'IR' and the 'KIN' methods. The EGF corrections are described in sections 2 and 5.

Simulations with the 'KIN' method		**Simulations with the 'IR' method**	
KIN01	with all the EGF Corrections	IR01	with rupture area[1] and rise time[2] from Irikura recipe
KIN02	without the f_{max} correction	IR02	with rupture area[1] from Irikura recipe and rise time[2] from Dujardin et al. (2020)
KIN03	without the radiation pattern correction	IR03	with rupture area[1] from Dujardin et al. (2020) and rise time[2] from Irikura recipe
KIN04	without the radiation pattern correction neither the f_{max} correction	IR04	with rupture area[1] and rise time[2] from Dujardin et al. (2020)

[1]: The rupture area from Irikura recipe is about 229 km² and from Dujardin et al. (2020) is about 135 km².

[2]: The rise time from Irikura recipe is estimated based on HERP (2017) and is equal to 0.78 s. The rise time from Dujardin et al. (2020) is estimated based on Somerville et al. (1999) and is equal to = 0.45 s.

For the eight simulations listed in Table 4, ground motions are simulated at stations CA02 and CA04 (Fig. 1). The simulated ground motions are analyzed in both the time and the frequency domains using several ground-motion Intensity Measures (Ims), including Arias Intensity (AI), Ground Motion Duration (DAI or $D_{5/95}$), Peak Ground Acceleration (PGA), Peak Ground Velocity (PGV), the Spectral Acceleration at 1 Hz (SA (1 Hz)) and at 3 Hz (SA (3 Hz)), and Fourier amplitude spectrum (FAS). The FAS are smoothed with the method by Konno and Ohmachi (1998), using a bandwidth parameter b = 40. Figure 7 compares the Fourier Amplitude Spectra (FAS) of the simulated ground motions. The differences between the FAS simulated using the two techniques and the various parameter configurations depend on the considered frequency range, station and component.

Regarding the IR method, the IR2 simulations exhibit higher Fourier amplitudes than the IR1 simulations above frequencies of approximately 1.5–2 Hz (i.e., 1/Trise). This difference arises because IR1 is characterized by a shorter rise time. Such behavior is consistent with the findings of Pitarka et al. (2017), who showed that decreasing the rise time compresses the radiated energy into a shorter pulse, thereby enhancing ground-motion amplitudes in the intermediate-period range. Furthermore, within the IR framework, increasing the fault surface

area while keeping the target seismic moment constant necessarily reduces the average slip and redistributes the seismic moment between asperities and the background region. This results in larger but less energetic asperities, together with an expanded background area characterized by longer slip durations. Consequently, the Fourier spectra tend to exhibit reduced high-frequency amplitudes and weaker intermediate-period energy - typically controlled by asperities - along with a relative increase in low-frequency energy associated with the enlarged background contribution. This explains why the IR3 simulations display relatively larger Fourier amplitudes in the ~ 2–20 Hz frequency range compared to the IR1 configurations.

For the 'KIN' method, the impact of the cut-off frequency f_{max} correction is clearly observed at high frequencies (simulations KIN01 and KIN03 compared with KIN02 and KIN04). Conversely, the radiation pattern correction affects only the low frequencies, particularly the EW component (KIN01 and KIN02 compared with KIN03 and KIN05). Note that the radiation pattern correction appears to be highly sensitive to both the considered component and selected station.

Figure A1 show, for the 3 components (EW: East-West; NS: North-South; Z: Up-Down), the acceleration time series recorded during the 2010 earthquake (2010 EGF) and calculated using the two configurations KIN03 and IR04 that are most consistent in terms of input parameters and correction options. As expected, the time series obtained by both the KIN03 and IR04 methods are very similar to the EGF recordings in terms of duration and the signal envelop shapes.

For these two comparable simulations KIN03 and IR04, the resulting Fourier Amplitude Spectra (FAS) are very similar above approximately 2 Hz. The small differences can be attributed to the random components included in the rupture time, differences in slip distributions and different shapes of the slip rate functions. Below 2 Hz, however, the IR method yields larger Fourier amplitudes than the KIN method, particularly at station CA02 and for the north component. These results indicate that, when rise time and slip distribution are calibrated according to the KIN parameterization, the IR method is capable of reproducing high-frequency ground motions that are comparable to those obtained with the KIN method, while some discrepancies remain in the low-frequency range.

Figure A2 represents, for both stations CA02 and CA04, the FAS of the 2010 EGF three components' recordings and the Moment rate amplitude functions between 1 and 35 Hz used by the two approaches. The differences observed between the two methods are correlated to the differences between the KIN03 and IR04 moment rate amplitude functions. In addition, the different behaviors between CA02 and CA04, on the East-West component for example, may be due to the frequency contents of the EGF recordings. For CA02, located on rock condition, the main energy is between 10 and 20 Hz. However, for CA04 located on soft soil, the main energy is between 5 and 10 Hz.

Figure 8 compares ground-motion intensity measures (PGA, PGV, Arias Intensity, Duration and Spectral Accelerations at 1 and 3Hz) computed at stations CA02 and CA04 using the KIN03 and IR04 simulations. As observed for the FAS, the largest differences between the two methods occur for the parameters that are mainly controlled by low frequency ground motion content: PGV, SA (1Hz) and SA (3Hz). Other differences remain limited. Notably, Arias Intensity, Duration and PGA, both strongly correlated with high-frequency ground-motion content (e.g., Campbell and Bozorgnia, 2012, 2019), are very similar for KIN03 and IR04.

Table 5 shows the geometric standard deviations of the different Intensity Measures analyzed in this section (PGA, PGV, Arias Intensity, Duration and Spectral Accelerations at 1 and 3Hz) estimated using different empirical models from the literature (Pedron et al., 2003; Berges-Thierry et al., 2003; Cauzzi et al., 2014; Boore et al.,2020; Kotha et al., 2020). As per this Table, the average IMs' variability is almost equal to 2.12, and the duration seems to have the smallest variability. The differences between IR04 and KIN03 are, except may be for parameters controlled by low frequencies, much lower than the variabilities from empirical models.

This comparison provides insight into the epistemic uncertainty associated with the choice of EGF-based simulation method. Importantly, this epistemic uncertainty related to the methodological choice is smaller than the aleatory uncertainty due to rupture variability, as shown in section 3.

Table 5

The geometric standard deviations ($10^{\sigma(log_{10}(IM))}$) of different Intensity Measures (PGA – Peak Ground Acceleration, PGV – Peak Ground Velocity, AI – Arias Intensity and $D_{5/95}$ – Duration between 5–95% of the total signal energy, SA (1 Hz) – Spectral Acceleration at 1 Hz, SA (3 Hz) – Spectral Acceleration at 3 Hz) estimated for a Mw 6.0 event using different ground motion prediction equations (GMPEs) from the literature (Pedron et al., 2003; Berges-Thierry et al., 2003; Cauzzi et al., 2014; Boore et al.,2020; Kotha et al., 2020).

Intensity Measures	**Standard deviation**				
	Pedron et al. (2003)	**Berges-Thierry et al. (2003)**	**Cauzzi et al. (2014)**	**Boore et al. (2020))**	**Kotha et al. (2020)**
SA (1Hz)	N/A	1.96	2.37	2.20	2.19
SA (3Hz)	N/A	2.23	2.29	2.05	2.16
PGA	2.04	1.97	2.17	2.00	2.12
PGV	2.19	N/A	2.10	2.00	2.05
AI	2.65	N/A	N/A	N/A	N/A
$D_{5/95}$	1.60	N/A	N/A	N/A	N/A

6. Conclusion

This study examines the robustness of near-fault strong-motion predictions based on Empirical Green's Functions (EGFs) for a Mw 6 scenario on the Middle Durance Fault and ranks the uncertainties associated with the input parameters (e.g., source and EGF parameters), the number of available EGFs, and the EGF-based technique used in the calculations. In this work, the rupture area is assumed to be fixed, and ground motions are simulated at two sites located approximately 7 km from the fault in the Cadarache area. One site corresponds to rock conditions (station CA02), whereas the second site (station CA04) lies within the small three-dimensional sedimentary basin of Cadarache (Fig. 1). The simulations rely on a single Mw 2.8 earthquake recorded in 2010 as the reference EGF event. The main modelling strategy adopted in this study incorporates a detailed representation of rupture kinematics (Dujardin et al., 2020; Causse et al., 2021).

We find that the overall ground-motion variability -including variability in rupture and EGF parameters - remains slightly larger (factor ~ 2.7) than typical values reported in empirical ground-motion models (generally < 2.5), highlighting epistemic uncertainties specific to EGF-based predictions (Al-Atik et al., 2010). Using an ensemble

machine-learning algorithm, we show that the EGF source parameters exert the largest influence on the predictions. In particular, the EGF seismic moment primarily controls the overall amplitude scaling, whereas the EGF stress drop mainly influences the high-frequency content of the motions, including PGA and short-period spectral accelerations. The nucleation position also contributes to variability in the near-fault region. High-frequency ground motion is strongly sensitive to rupture velocity; however, because the epistemic uncertainty associated with rupture velocity is relatively limited compared with other parameters, its contribution to the overall variability remains moderate.

Using three-dimensional numerical simulations for the main rupture scenarios, together with point-source simulations mimicking EGFs, we show that the configuration of the EGF dataset has a secondary influence, particularly at frequencies below ~ 1 Hz. The results indicate that the spatial distribution of EGFs across the rupture area is more critical than their number: a limited but well-distributed set reproduces the reference waveforms and response spectra satisfactorily, whereas EGFs located at unfavorable positions degrade the predictions. Notably, a single EGF located as close as possible to the station can already provide reliable predictions.

Finally, methodological differences between the Irikura recipe—a widely used EGF approach—and the k-square extended-source approach produce comparable results above ~ 2 Hz. The main discrepancies appear in the 1–2 Hz band and are primarily related to differences in the moment-rate functions.

Because the study area is located in the low-seismicity Middle Durance region, these results would benefit from further validation in more seismically active areas where a larger number of small earthquakes is available. Such datasets would allow a more systematic comparison with observed records and help better constrain the physical processes controlling the simulated ground motions. More broadly, integrating EGF-based simulations within physics-informed, non-ergodic uncertainty frameworks could help distinguish epistemic from aleatory variability and improve the reliability of scenario-based ground-motion predictions (Valentová et al., 2021; Maufroy et al., 2016).

Declarations

Author Contribution

EEH and MC wrote the main manuscript textLSM did the Irikura calculationsDCC did the PBS simulations using the SEM3D softwareEEH did all KIN simulationsEEH and MC did the comparisons and figuresFH provides all the required data and reviwed the workAll authors reviewed the paper

Acknowledgement

This study was carried out under the Sinaps@ project that received French funding managed by the French National Research Agency under the program “Future Investments” (Sinaps@ reference: ANR-11- RSNR-022-04). Sinaps@ is a “Seism Institute” project (https://www.institut-seism.fr/projets/sinaps/, last accessed June 2025).

8. Data availability

The used python code to generate strong ground motion using 'IR' method have been developed by EDF R&D team in collaboration with CRIEPI and is available on gitlab (https://github.com/LudivineSaintMard/IR-GMS). The Matlab code used to generate the KIN simulations is available in the supplementary elements of the paper.

References

1. Abercrombie, R. E. (2015). Investigating uncertainties in empirical Green's function analysis of earthquake source parameters. *Journal of Geophysical Research: Solid Earth*, *120*(6), 4263–4277.
2. Abercrombie, R. E., Shearer, P. M., Trugman, D. T., & Wang, W. (2019). Comparing EGF methods for estimating corner frequency and stress drop from P-wave spectra. *Journal of Geophysical Research: Solid Earth*, *124*(5), 3966–3986.
3. Aki, K., & Richards, P. G. (1980). *Quantitative Seismology*. W. H. Freeman.
4. Al-Atik, L., Abrahamson, N., Bommer, J. J., Scherbaum, F., Cotton, F., & Kuehn, N. (2010). The variability of ground-motion prediction models and its components. *Seismological Research Letters*, *81*(5), 794–801.
5. Anderson, J. G., & Brune, J. N. (1999). Probabilistic seismic hazard analysis without the ergodic assumption. *Seismological Research Letters*, *70*(1), 19–28.
6. Anderson, J. G., & Hough, S. E. (1984). A model for the shape of the Fourier amplitude spectrum of acceleration at high frequencies. *Bulletin of the Seismological Society of America*, *74*(5), 1969–1993.
7. Andrews, D. J., 1980, A stochastic fault model: 1. Static case, Journal of Geophysical Research: Solid Earth, 85, no. B7, 3867–3877, doi: 10.1029/JB085iB07p03867.
8. Arias, A. (1970). A measure of earthquake intensity. In R. J. Hansen (Ed.), *Seismic Design for Nuclear Power Plants* (pp. 438–483). MIT Press.
9. Baroux, E., Pino, N. A., Valensise, G., Scotti, O., & Cushing, M. E. (2003). Source parameters of the 11 June 1909, Lambesc (Provence, SE France) earthquake: A reappraisal based on macroseismic, seismological, and geodetic observations. *Journal of Geophysical Research: Solid Earth*, *108*(B9), 2454.
10. Berge-Thierry, C., Cotton, F., Scotti, O., Griot-Pommera, D. A., & Fukushima, Y. (2003). New empirical response spectral attenuation laws for moderate European earthquakes. *Journal of Earthquake Engineering*, *7*(02), 193–222.
11. Boore, D. M. (1983). Stochastic simulation of high-frequency ground motions based on seismological models of the radiated spectra. *Bulletin of the Seismological Society of America*, *73*(6), 1865–1894.
12. Boore, D. M., Stewart, J. P., Skarlatoudis, A. A., Seyhan, E., Margaris, B., Theodoulidis, N., … Melis, N. S. (2021). A ground-motion prediction model for shallow crustal earthquakes in Greece. *Bulletin of the Seismological Society of America*, *111*(2), 857–874.
13. Brune, J. N. (1970). Tectonic stress and the spectra of seismic shear waves from earthquakes. *Journal of Geophysical Research*, *75*(26), 4997–5009.
14. Campbell, K. W., & Bozorgnia, Y. (2012). A comparison of NGA-West and NGA-West2 ground-motion prediction equations. *Earthquake Spectra*, *28*(3), 979–1010.
15. Campbell, K. W., & Bozorgnia, Y. (2019). Updated NGA-West2 ground-motion model for horizontal components of PGA, PGV, and 5%-damped response spectra. *Earthquake Spectra*, *35*(4), 1889–1920.
16. Causse, M., & Song, S. G. (2015). Effects of an anticorrelation between stress drop and rupture velocity on near-source ground-motion variability. *Geophysical Journal International*, *200*(2), 1101–1112.

17. Causse, M., G. Cultrera, L. Moreau, A. Herrero, E. Schiappapietra, and F. Courboulex, 2017, Bayesian rupture imaging in a complex medium. The 29 May 2012 Emilia, Northern Italy, earthquake: Rupture imaging in a complex medium, Geophysical Research Letters, doi: 10.1002/2017GL074698.
18. Causse, M., E. Chaljub, F. Cotton, C. Cornou, and P.-Y. Bard, 2009, New approach for coupling k – 2 and empirical Green's functions: application to the blind prediction of broad-band ground motion in the Grenoble basin, Geophys J Int, 179, no. 3, 1627–1644, doi: 10.1111/j.1365-246X.2009.04354.x.
19. Causse, M., E. Maufroy, L. André, and P.-Y. Bard, 2023, What Was the Level of Ground Motion across Europe during the Great A.D. 365 Crete Earthquake?, Seismological Research Letters, doi: 10.1785/0220220385.
20. Cauzzi, C., Faccioli, E., Vanini, M., & Bianchini, A. (2015). Updated predictive equations for broadband (0.01–10 s) horizontal response spectra and peak ground motions, based on a global dataset of digital acceleration records. Bulletin of Earthquake Engineering, 13(6), 1587–1612.
21. Castro-Cruz, D., Gatti, F., & Lopez-Caballero, F. (2021). High-fidelity broadband prediction of regional seismic response: A hybrid coupling of physics-based synthetic simulation and empirical Green functions. *Natural Hazards*, *108*, 1997–2031.
22. Castro-Cruz, D., Gatti, F., Lopez-Caballero, F., Hollender, F., El Haber, E., & Causse, M. (2023). Blind broad-band (0–10 Hz) numerical prediction of the 3-D near-field seismic response of a Mw 6.0 extended fault scenario: Application to the nuclear site of Cadarache (France). *Geophysical Journal International*, *232*(1), 581–600.
23. Čejka, F., Sgobba, S., Pacor, F., Felicetta, C., Valentová, Ľ., & Gallovič, F. (2024). Constraining between-event variability of kinematic rupture scenarios by empirical ground-motion model: A case study in central Italy. *Bulletin of the Seismological Society of America*, *114*(4), 2138–2150.
24. Chounet, A., Vallée, M., Causse, M., & Courboulex, F. (2018). Global catalog of earthquake rupture velocities shows anticorrelation between stress drop and rupture velocity. *Tectonophysics*, *733*, 148–158.
25. Courboulex, F., Dujardin, A., Vallée, M., Delouis, B., Sira, C., Deschamps, A., Honoré, L., & Thouvenot, F. (2013). High-frequency directivity effect for an Mw 4.1 earthquake, widely felt in southeastern France. *Bulletin of the Seismological Society of America*, *103*(6), 3347–3353.
26. Courboulex, F., Vallée, M., Causse, M., & Chounet, A. (2016). Stress-drop variability of shallow earthquakes extracted from a global database of source time functions. *Seismological Research Letters*, *87*(4), 912–918.
27. Cotton, F., Scherbaum, F., Bommer, J. J., & Stafford, P. J. (2013). Toward better estimations of ground-motion variability. *Seismological Research Letters*, *84*(6), 1111–1121.
28. Cultrera, G., Cirella, A., Spagnuolo, E., Herrero, A., Tinti, E., & Pacor, F. (2010). Variability of kinematic source parameters and its implication on the choice of the design scenario. *Bulletin of the Seismological Society of America*, *100*(3), 941–953.
29. Das, S., & Kostrov, B. V. (1986). Fracture of a single asperity on a finite fault. In *Earthquake Source Mechanics* (Geophysical Monograph 37, Maurice Ewing Series 6, pp. 91–96). American Geophysical Union.
30. Del Gaudio, S., Causse, M., & Festa, G. (2015). Broad-band strong motion simulations coupling k-square kinematic source models with empirical Green's functions: the 2009 L'Aquila earthquake. *Geophysical Journal International*, *203*(1), 720–736.
31. Del Gaudio, S., Causse, M., Festa, G., Hok, S., & Lancieri, M. (2018). Near fault broadband ground motion simulation using empirical Green's functions: application to L'Aquila (Italy) and Upper Rhine Graben (France-Germany) cases of study. In *Best Practices in Physics Based Fault Rupture Models for Seismic Hazard*

Assessment of Nuclear Installations. Proceedings of a Workshop (No. IAEA-TECDOC-CD–1833, pp. 125–136).

32. Dujardin, A., Hollender, F., Causse, M., Berge-Thierry, C., Delouis, B., Foundotos, L., Ameri, G., & Shible, H. (2020). Optimization of a simulation code coupling extended source (k-2) and empirical Green's functions: Application to the Middle Durance Fault. *Pure and Applied Geophysics*, *177*(5), 2255–2279.
33. Eshelby, J. D. (1957). The determination of the elastic field of an ellipsoidal inclusion, and related problems. *Proceedings of the Royal Society A, 241*(1226), 376–396.
34. Faccioli, E., Maggio, F., Paolucci, R., & Quarteroni, A. (1997). 2-D and 3-D elastic wave propagation by a pseudo-spectral domain decomposition method. *Journal of Seismology*, *1*(3), 237–251.
35. Fayjaloun, R., Causse, M., Cornou, C., Voisin, C., & Song, S. G. (2019). Sensitivity of high-frequency ground motion to kinematic source parameters. *Pure and Applied Geophysics*, *177*(5), 1947–1967.
36. Festa, G., & Vilotte, J.-P. (2005). The Newmark scheme as velocity–stress time-staggering: An efficient PML implementation for spectral element simulations of elastodynamics. *Geophysical Journal International*, *161*(3), 789–812.
37. Guyonnet-Benaize, C., Lamarche, J., Hollender, F., Viseur, S., M˙unch, P., & Borgomano, J. (2015). Three-dimensional structural modeling of an active fault zone based on complex outcrop and subsurface data: The Middle Durance Fault Zone inherited from polyphase Meso-Cenozoic tectonics (southeastern France). Tectonics, 34(2), 265–289.
38. Hanks, T. C. (1982). fmax. *Bulletin of the Seismological Society of America, 72*(6A), 1867–1879.
39. Hartzell, S. (1978). Earthquake aftershocks as Green's functions. *Geophysical Research Letters*, *5*(1), 1–4.
40. Heaton, T. H. (1990). Evidence for and implications of self-healing pulses of slip in earthquake rupture. *Physics of the Earth and Planetary Interiors*, *64*(1), 1–20.
41. Herrero, A., and P. Bernard, 1994, A kinematic self-similar rupture process for earthquakes, Bulletin of the Seismological Society of America, 84, no. 4, 1216–1228, doi: 10.1785/BSSA0840041216.
42. HERP (Headquarters for Earthquake Research Promotion). (2017). *Strong ground motion prediction method for earthquakes with specified source faults ("Recipe")* (April, in Japanese).
43. Honoré, L., Courboulex, F., & Souriau, A. (2011). Ground-motion simulations of a major historical earthquake (1660) in the French Pyrenees using recent moderate-size earthquakes. *Geophysical Journal International*, *186*(3), 1–20.
44. Hutchings, L., & Viegas, G. (2012). Application of Empirical Green's Functions in earthquake source, wave propagation and strong ground-motion studies. In S. D'Amico (Ed.), *Earthquake Research and Analysis – New Frontiers in Seismology*. InTech.
45. Hutchings, L., & Wu, F. (1990). Empirical Green's functions from small earthquakes: A waveform study of aftershocks of the 1971 San Fernando earthquake. *Journal of Geophysical Research*, *95*(B10), 11875–11896.
46. Hutchings, L. (1994). Kinematic earthquake models and synthesized ground motion using empirical Green's functions. *Bulletin of the Seismological Society of America*, *84*(4), 1028–1050.
47. Irikura, K. (1983). Semi-empirical estimation of strong ground motions during large earthquakes. *Bulletin of the Disaster Prevention Research Institute*, *33*(2), 229–239.

48. Irikura, K. (1986). Prediction of strong acceleration motions using empirical Green's function. *Proceedings of the 7th Japan Earthquake Engineering Symposium*, 151–156.
49. Irikura, K., & Kamae, K. (1994). Estimation of strong ground motion in broad frequency band using a hybrid technique combining empirical and theoretical Green's functions. *Zisin (Journal of the Seismological Society of Japan)*, *46*, 1–13. (en japonais, résumé en anglais)
50. Irikura, K., & Miyake, H. (2011). Recipe for predicting strong ground motion from crustal earthquake scenarios. *Pure and Applied Geophysics*, *168*(1–2), 85–104.
51. Irikura, K., Kagawa, T., & Sekiguchi, H. (1997). Revision of the empirical Green's function method. *Programme and Abstracts, Seismological Society of Japan*, *2*, B25–B28.
52. Irikura, K., Miyake, H., Iwata, T., Kamae, K., Kawabe, H., & Dalguer, L. A. (2004). Recipe for predicting strong ground motion from future large earthquake. In *Proceedings of the 13th World Conference on Earthquake Engineering* (No. 1371).
53. Kanamori, H., & Anderson, D. L. (1975). Theoretical basis of some empirical relations in seismology. *Bulletin of the Seismological Society of America*, *65*(5), 1073–1095.
54. Kohrs-Sansorny, C., Courboulex, F., Bour, M., & Deschamps, A. (2005). A two-stage method for ground-motion simulation using stochastic summation of small earthquakes. *Bulletin of the Seismological Society of America*, *95*(4), 1387–1400.
55. Komatitsch, D., & Vilotte, J.-P. (1998). The spectral element method: An efficient tool to simulate the seismic response of 2-D and 3-D geological structures. *Bulletin of the Seismological Society of America*, *88*(2), 368–392.
56. Konno, K., & Ohmachi, T. (1998). Ground-motion characteristics estimated from spectral ratio between horizontal and vertical components of microtremor. *Bulletin of the Seismological Society of America*, *88*(1), 228–241.
57. Kotha, S. R., Weatherill, G., Bindi, D., & Cotton, F. (2020). A regionally-adaptable ground-motion model for shallow crustal earthquakes in Europe. *Bulletin of Earthquake Engineering*, *18*(9), 4091–4125.
58. Madariaga, R. (1977). High-frequency radiation from crack (stress drop) models of earthquake faulting. *Geophysical Journal of the Royal Astronomical Society*, *51*(3), 625–652.
59. Madariaga, R. (1979). On the relation between seismic moment and stress drop in the presence of stress and strength heterogeneity. *Journal of Geophysical Research*, *84*(B5), 2243–2250.
60. Mai, P. M., Schorlemmer, D., Page, M. T., Ampuero, J.-P., Asano, K., Causse, M., …Zielke, O. (2016). The Earthquake-Source Inversion Validation (SIV) Project. *Seismological Research Letters, 87*(3), 690–708.
61. Mai, P. M., Spudich, P., & Boatwright, J. (2005). Hypocenter locations in finite-source rupture models. *Bulletin of the Seismological Society of America*, *95*(3), 965–980.
62. Manchuel, K., Traversa, P., Baumont, D., Cara, M., Nayman, E., & Durouchoux, C. (2018). The French seismic CATalogue (FCAT-17). *Bulletin of Earthquake Engineering*, *16*(6), 2227–2251.
63. Maufroy, E., Chaljub, E., Hollender, F., et al. (2015). Earthquake ground motion in the Mygdonian basin, Greece: The E2VP verification and validation of 3-D numerical simulation up to 4 Hz. *Bulletin of the Seismological Society of America*, *105*(3), 1398–1418.
64. Maufroy, E., Chaljub, E., Hollender, F., Bard, P.-Y., Kristek, J., Moczo, P., … Pitilakis,K. (2016). 3-D numerical simulation and ground-motion prediction: Verification, validation and beyond—Lessons from the E2VP

project. *Soil Dynamics and Earthquake Engineering, 91*, 53–71.

65. Miyake, H., Iwata, T., & Irikura, K. (2003). Source characterization for broadband ground-motion simulation: Kinematic heterogeneous source model and strong motion generation area. *Bulletin of the Seismological Society of America*, *93*(6), 2531–2545.
66. Mueller, C. S. (1985). Source pulse enhancement by deconvolution of an empirical Green's function. *Geophysical Research Letters*, *12*(1), 33–36.
67. Parker, G. A., M. P. Moschetti, and E. M. Thompson, 2023, Ground-Motion Variability from Kinematic Rupture Models and the Implications for Nonergodic Probabilistic Seismic Hazard Analysis, Seismological Research Letters, 94, no. 6, 2687–2697, doi: 10.1785/0220220380.
68. Pedron, C., Sollogoub, P., Goubet, S., & Viallet, E. (2003, August). Quantification of the effects of low magnitude near field earthquakes. In *Transactions of the 17th International Conference on Structural Mechanics in Reactor technology (SMiRT17), Prague, Czech Republic*.
69. Pitarka, A., Graves, R., Irikura, K., Miyake, H., & Rodgers, A. (2017). Performance of Irikura recipe rupture model generator in earthquake ground motion simulations with Graves and Pitarka hybrid approach. In *Best Practices in Physics-based Fault Rupture Models for Seismic Hazard Assessment of Nuclear Installations* (pp. 213–231). Cham: Springer International Publishing.
70. RESIF. (1995). *Réseau Sismologique et géodésique Français* — documentation réseau.
71. Ripperger, J., Mai, P. M., & Ampuero, J. P. (2008). Variability of near-field ground motion from dynamic earthquake rupture simulations. *Bulletin of the seismological society of America*, *98*(3), 1207–1228.
72. Ross, Z. E., Kanamori, H., & Hauksson, E. (2017). Anomalously large complete stress drop during the 2016 Mw 5.2 Borrego Springs earthquake inferred by waveform modeling and near-source aftershock deficit. *Geophysical Research Letters*, *44*(12), 5994–6001.
73. Schmedes, J., & Archuleta, R. J. (2008). Near-source ground-motion variability from heterogeneous earthquake ruptures. *Geophysical Journal International*, *172*(1), 26–41.
74. Shearer, P. M., Abercrombie, R. E., Trugman, D. T., & Wang, W. (2019). Voir entrée "Abercrombie et al., 2019".
75. Somerville, P., Irikura, K., Graves, R., Sawada, S., Wald, D., Abrahamson, N., Iwasaki, Y., Kagawa, T., Smith, N., & Kowada, A. (1999). Characterizing crustal earthquake slip models for the prediction of strong ground motion. *Seismological Research Letters*, *70*(1), 59–80.
76. Spudich, P., & Frazer, L. N. (1984). Use of ray theory to calculate high-frequency radiation from earthquake sources with spatially random rupture velocity. *Bulletin of the Seismological Society of America*, *74*(6), 2061–2082.
77. Stone, I., Wirth, E. A., Grant, A., & Frankel, A. D. (2025). High-Frequency and Region-Scale Simulations of Large (M w 7+) Earthquakes on the Southern Whidbey Island Fault, Washington, USA. *Bulletin of the Seismological Society of America*.
78. Tsurugi, K., Kagawa, T., & Irikura, K. (2017). Validation of two approaches for expressing spectral decay characteristics at high frequency: fmax and κ models. *Proceedings of the 16th World Conference on Earthquake Engineering* (Paper 1232).
79. Valentová, Ľ., Gallovič, F., & Hok, S. (2021). Near-source ground motions and their variability derived from dynamic rupture simulations constrained by NGA-West2 GMPEs. *Bulletin of the Seismological Society of America*, *111*(5), 2559–2573.

80. Wössner, J., Treml, M., & Wenzel, F. (2002). Simulation of Mw = 6.0 earthquakes in the Upper Rhinegraben using empirical Green functions. *Geophysical Journal International*, *151*(2), 487–500.

81. Žilić, I., Causse, M., Vallée, M., & Markušić, S. (2025). High stress drop and slow rupture during the 2020 MW6. 4 intraplate Petrinja Earthquake, Croatia. *Journal of Geophysical Research: Solid Earth*, *130*(1), e2024JB029107.

Figures

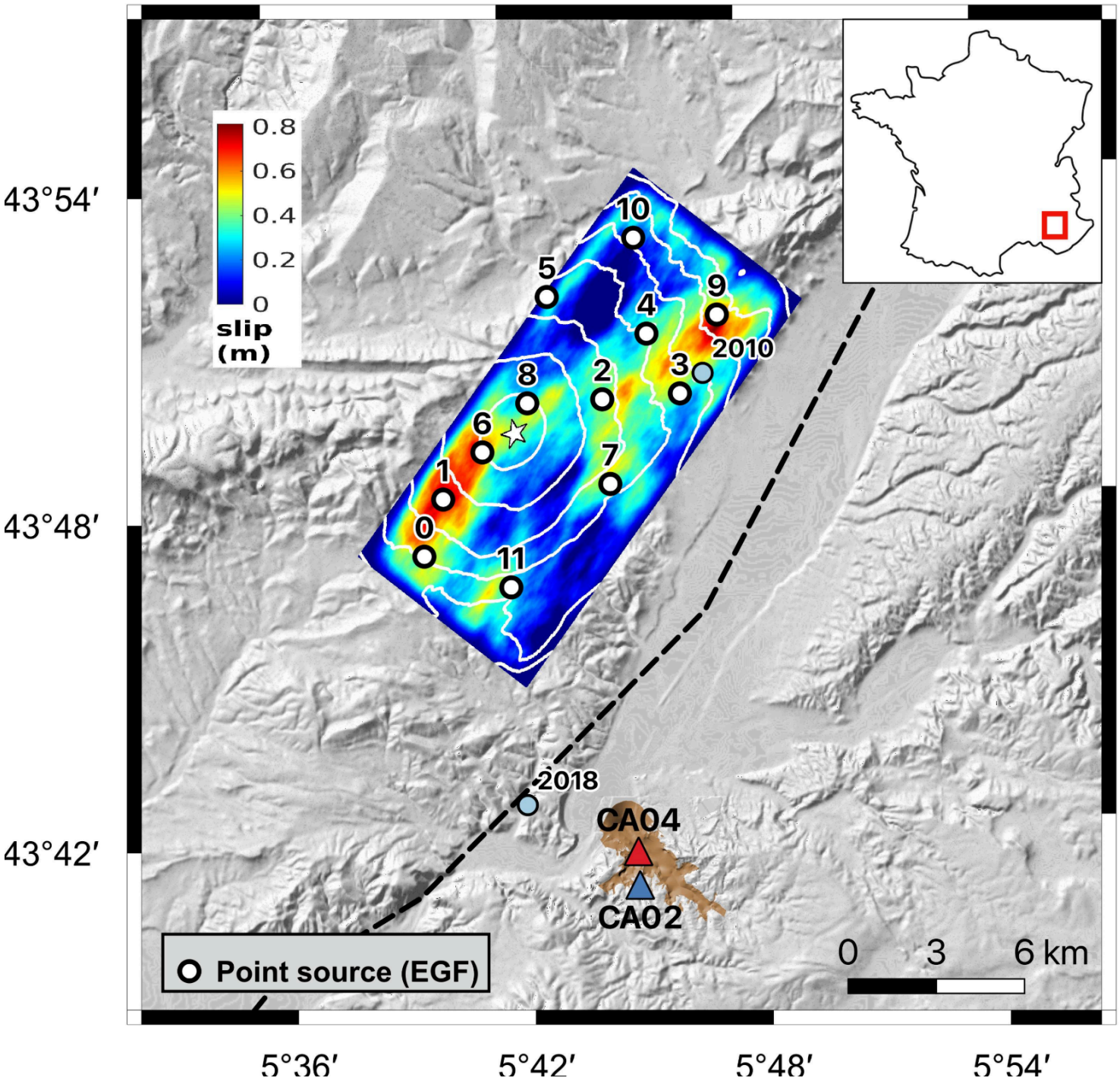


Figure 1

Map of the Cadarache area (Southeast of France) showing an example of rupture scenario for a M_w6 event. The blue dots correspond to the 2010 and 2018 small earthquakes that occurred on the Middle Durance Fault system. Only the 2010 event, located within the assumed rupture area, is used as EGF. The numbered white dots correspond to the synthetic events (point source) generated using SEM3D, see section 6 for details. The white star and isolines correspond, respectively, to the epicenter and the rupture time of this scenario. Simulations are performed at stations CA02 (located at rock) and CA04 (located within the small sedimentary basin, represented in brown). The black dashed line represents the trace of the MDF (Guyonnet-Benaize et al. 2015).

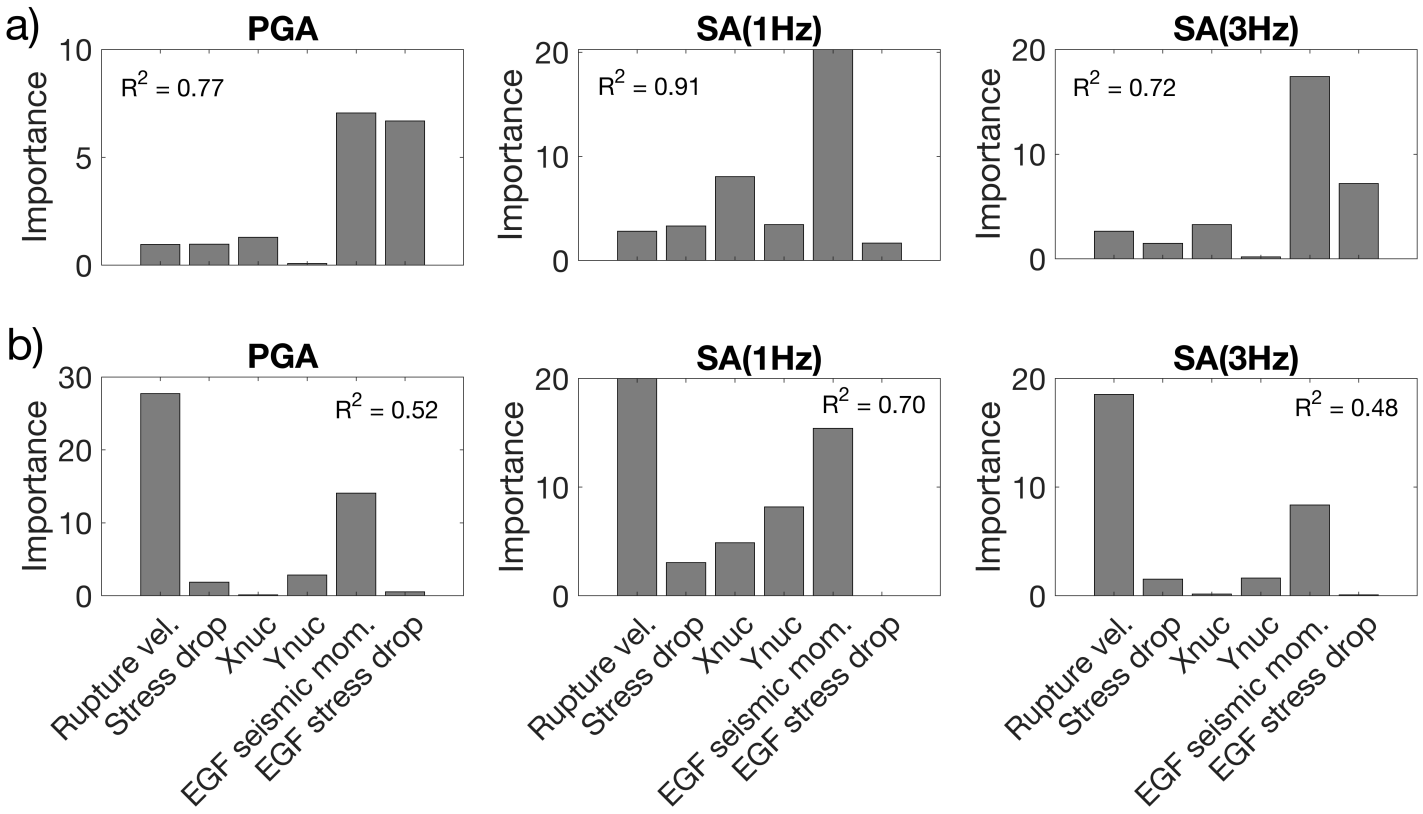


Figure 2

Importance of the predictors in the EGF ground motion simulations of a Mw6 event at rock station CA02. The importance is computed from 5000 rupture scenarios using: (a) the predictor probability distributions of Table 2; (b) a uniform distribution with a coefficient of variation equal to 0.18 for all the predictors. R^2 represents the coefficient of determination between the observations (subsets of simulated ground motions) and the predictions using bootstrap aggregation of regression trees.

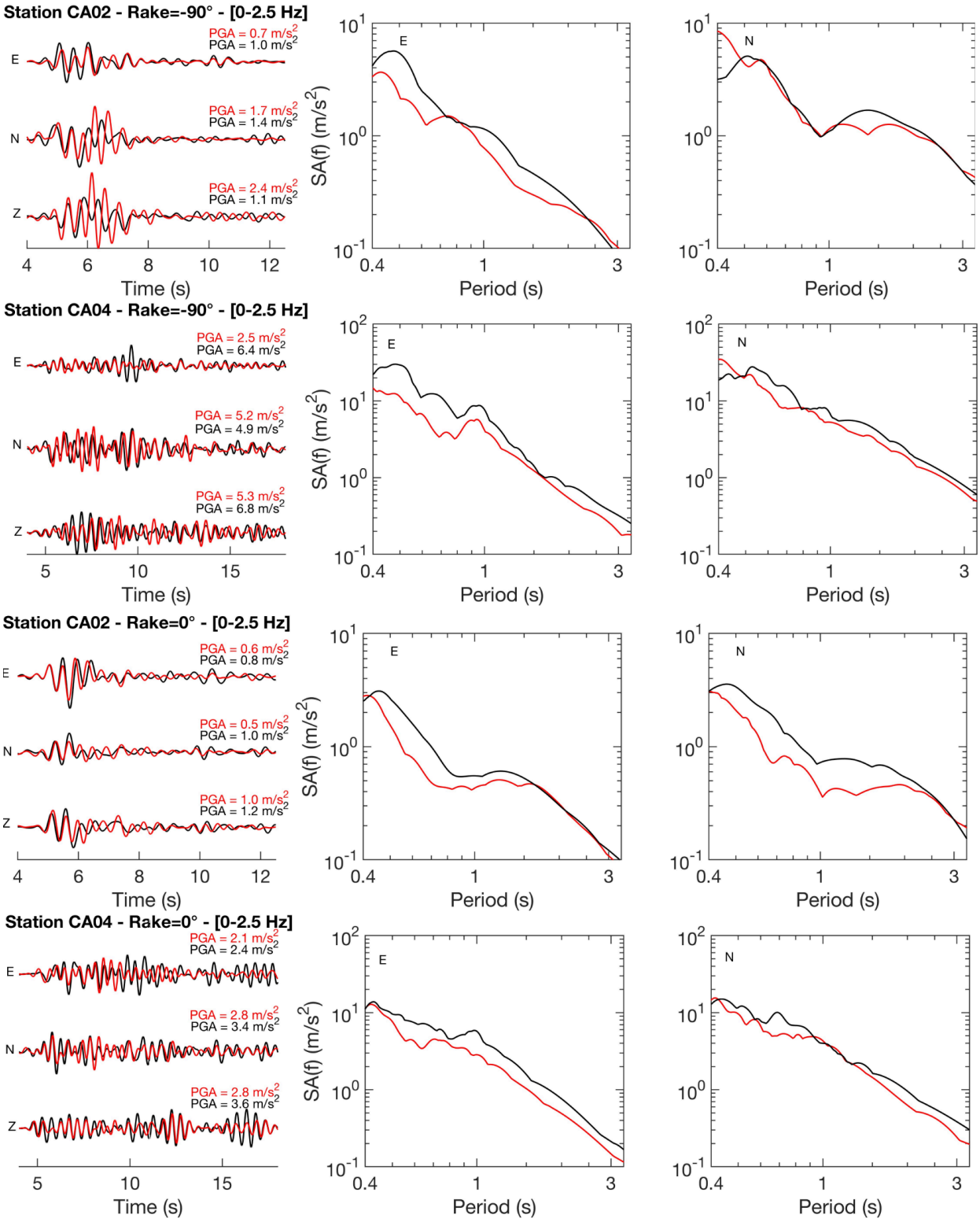


Figure 3

Comparison between reference numerical ground motion predictions and predictions using a set of 13 synthetic EGF. Left : acceleration time histories ; right: elastic response spectra. Predictions are performed at stations CA02 and CA04 considering the rupture model of Fig. 1. and two fault mechanisms (rake = 0° and rake=90°). The positions of the synthetic EGFs, computed as point sources, is shown in Fig. 1.

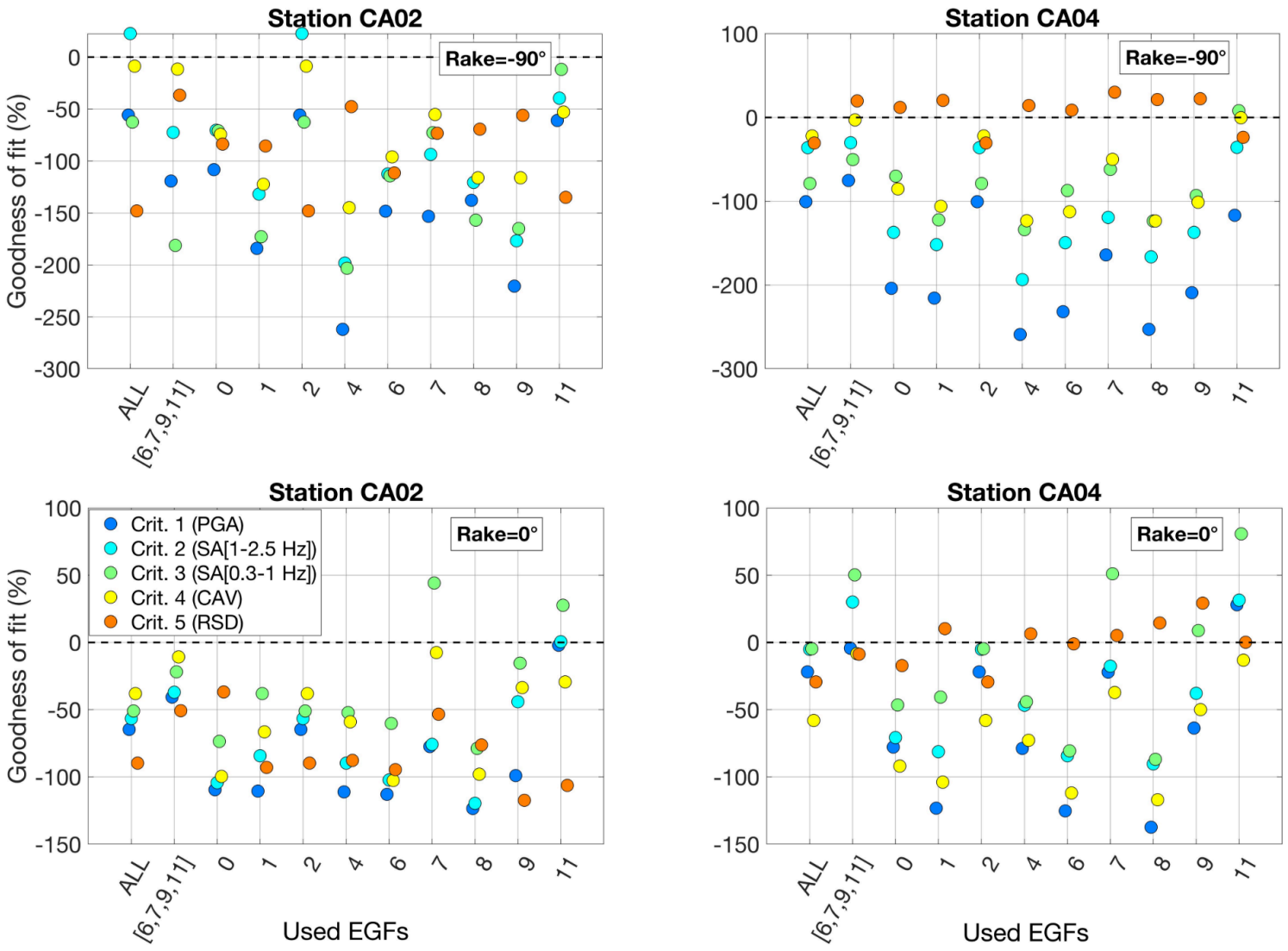


Figure 4

Comparison between reference numerical ground motion predictions and predictions based on EGF summation considering various sets of synthetic EGF. The synthetic EGF positions are displayed on Fig. 1. The results are shown for rake-angle values of -90° (top) and 0° (bottom).

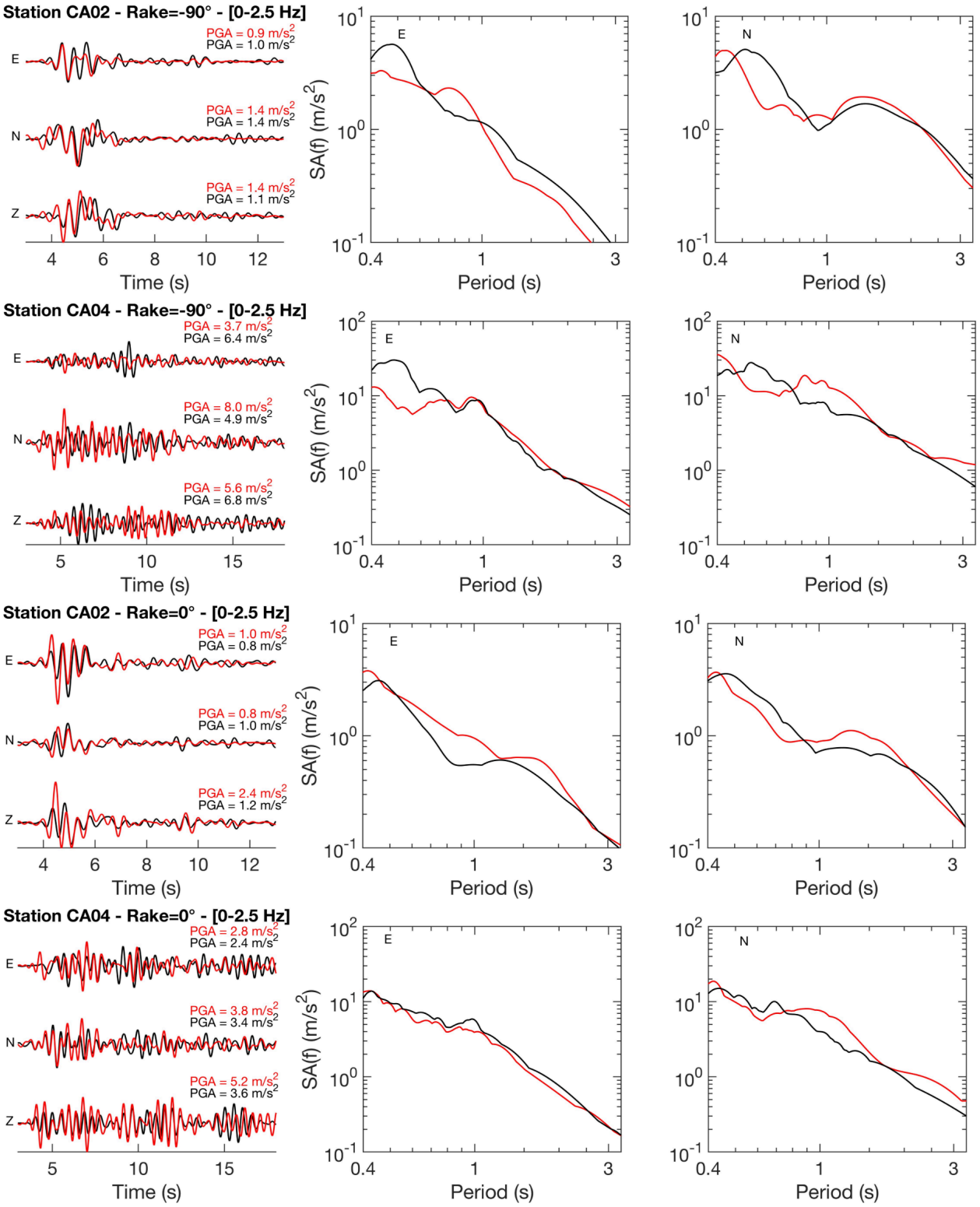


Figure 5

Comparison between reference numerical ground motion predictions and predictions using point source 11 as a unique synthetic EGF. The position of point source 11 is shown in Fig. 1. Left : acceleration time histories ; right: elastic response spectra. Predictions are performed at stations CA02 and CA04 considering the rupture model of Fig. 1. and two fault mechanisms (rake = 0° and rake=90°).

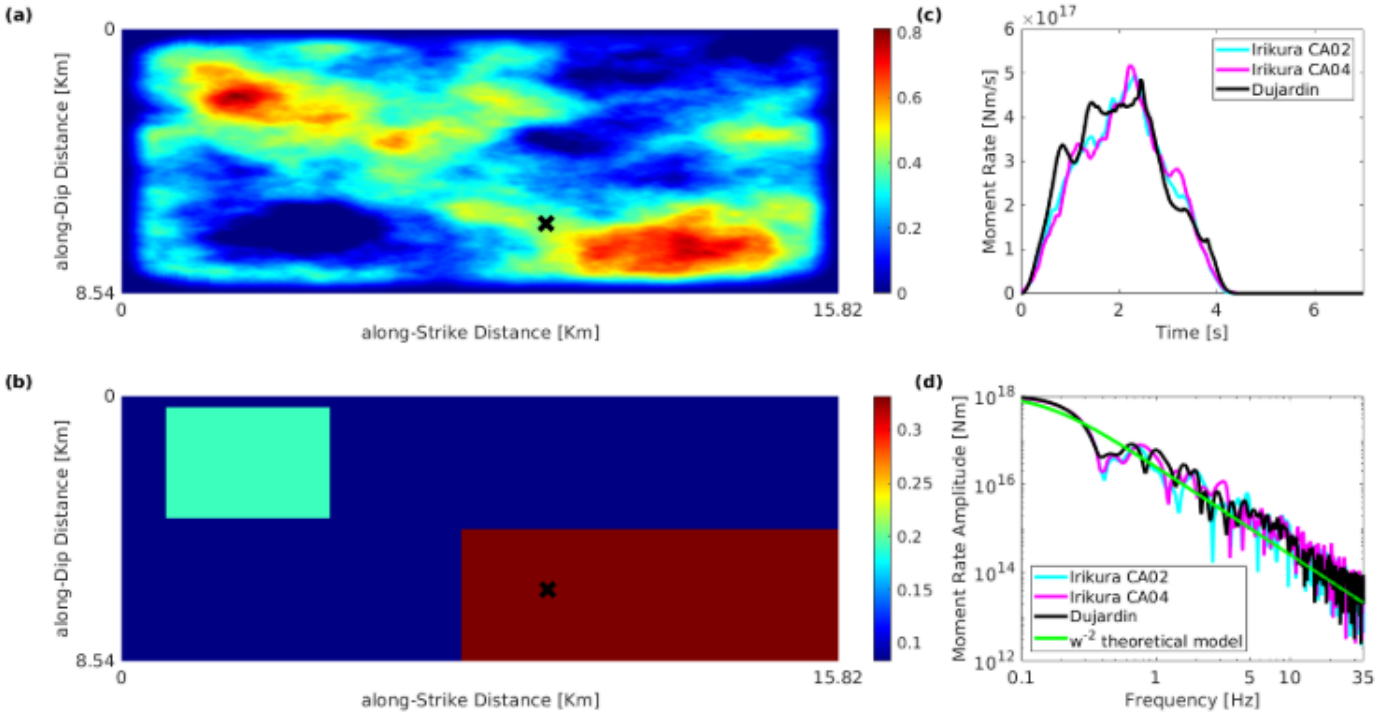


Figure 6

For one rupture scenario of an hypothetical Mw6.0 event on the Moyenne Durance Fault, the static slip distribution (a) generated by the Dujardin et al. (2020) simulation code and (b) constructed as per the Irikura Recipe to best-fit the slip distribution in (a) (refer to text for details) with the corresponding moment rate time function and amplitude defined for Trise = 0.45s (respectively, in (c) and (d)). The black crosses in (a) and (b) correspond to the nucleation position on the fault.The theoretical ω^2 spectra (Brune, 1970) computed for the medium value $\Delta\sigma$ = 0.79 MPa is represented by the green curve in (d).

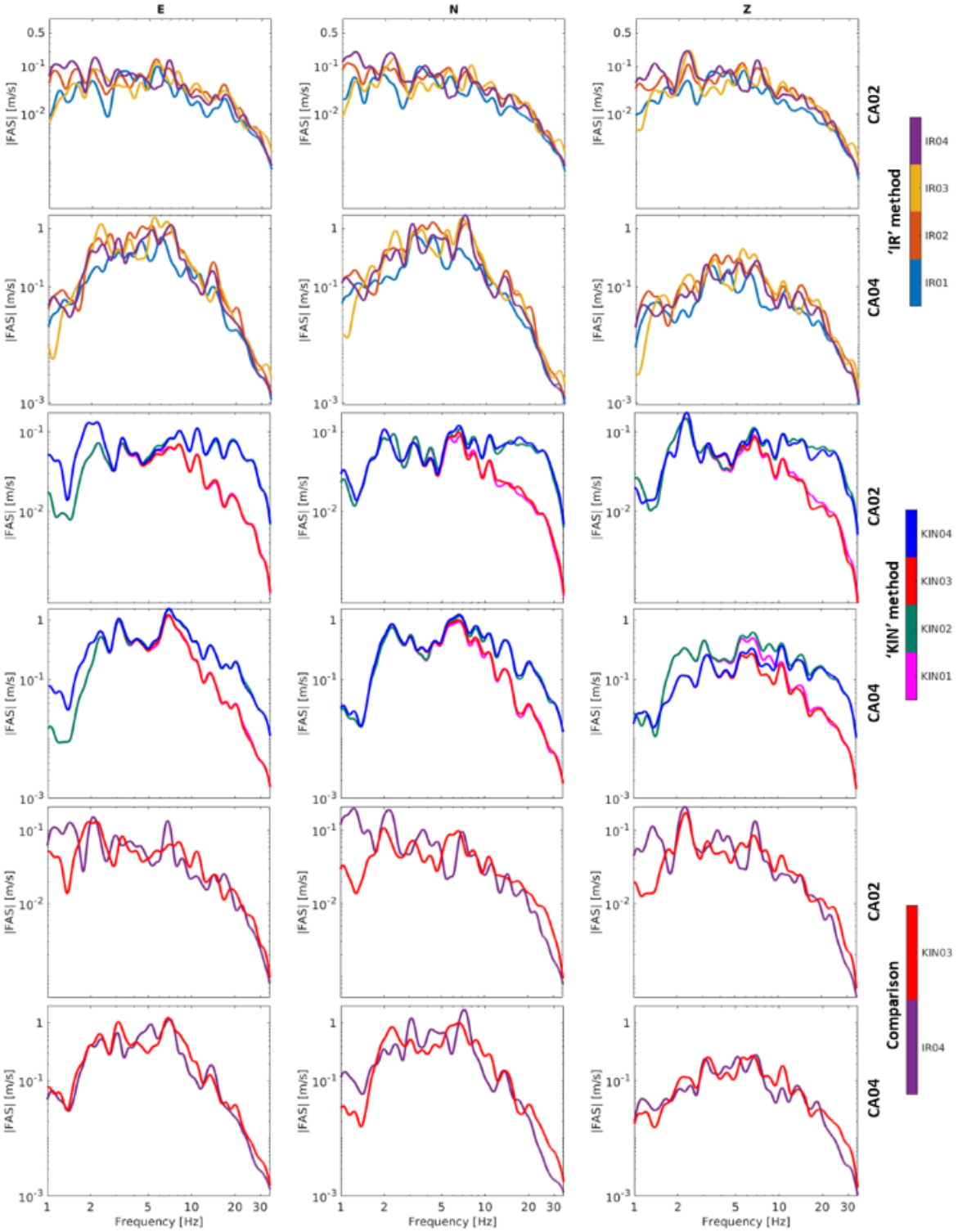


Figure 7

The Fourier Amplitude Spectrum (FAS) of three-component (E: East-West; N: North-South; Z: Up-Down) unfiltered acceleration time histories calculated by the eight different simulations (see Table 2 for details) and smoothed with the Konno and Ohmachi (b=40; Konno and Ohmachi, 1998), at two stations of the Cadarach Basin (CA02 and CA04). The ground motions simulated using the same method are grouped together (the first and second

rows for ‘IR’ simulations and the third and fourth rows for ‘KIN’ simulations) and for comparison, the results of the two simulations ‘IR04’ and ‘KIN03’ are shown in the last two rows of subplots

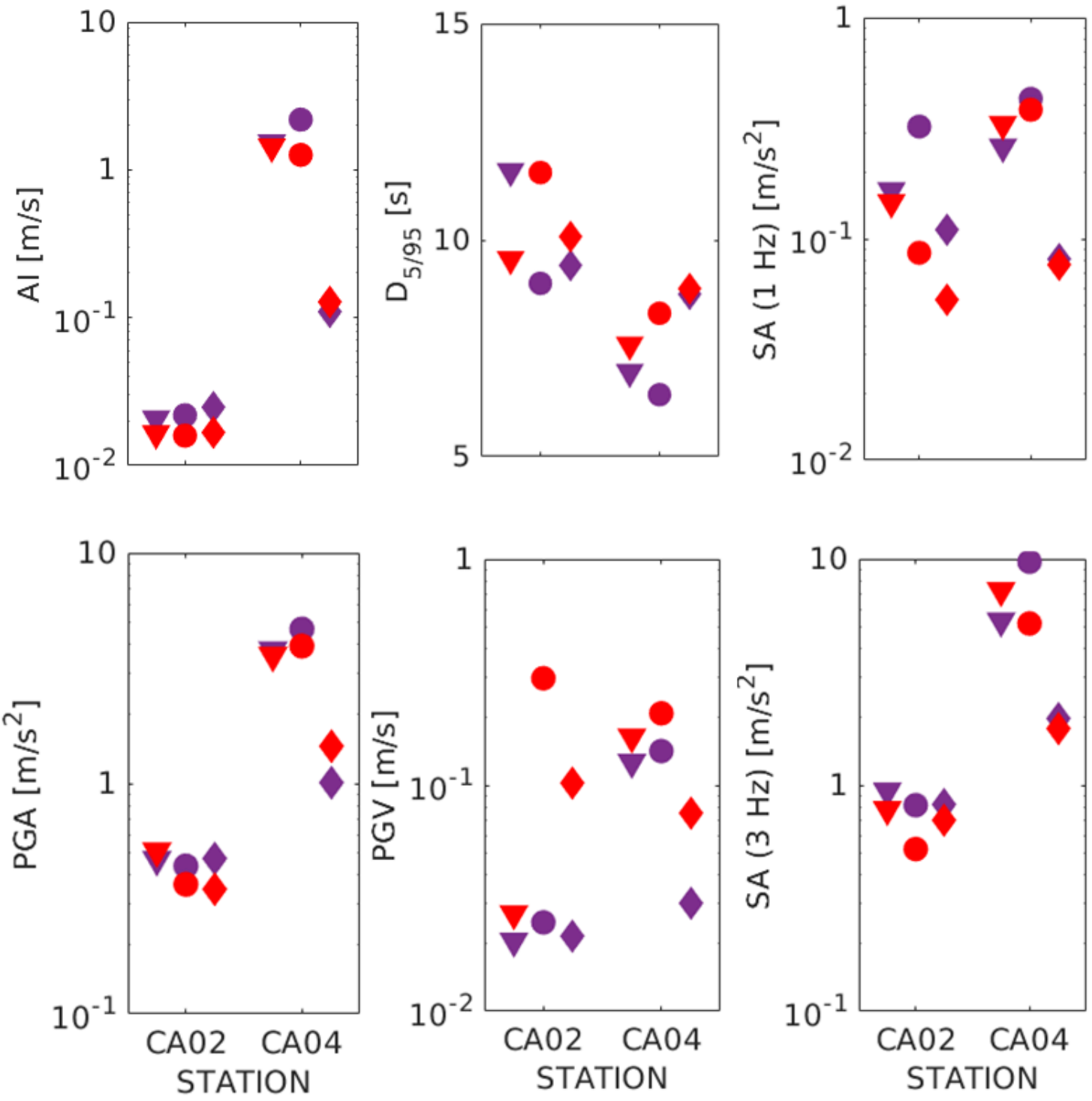


Figure 8

The ground motion intensity measures in the time domain (PGA – Peak Ground Acceleration, PGV – Peak Ground Velocity, AI – Arias Intensity and $D_{5/95}$ – Duration between 5-95% of the total signal energy, SA (1 Hz) – Spectral Acceleration at 1 Hz, SA (3 Hz) – Spectral Acceleration at 3 Hz) calculated within a frequency range between 1 and 35 Hz, by using the two simulations ‘IR04’ (in purple) and ‘KIN03’ (in red) (see text for details) for

the three components (Triangle: East-West; Circle: North-South; Diamond: Up-Down), at two stations of Cadarach basin (CA02 and CA04).

Supplementary Files

This is a list of supplementary files associated with this preprint. Click to download.

- floatimage9.png
- floatimage10.png